SCIENTIFIC REPORTS

OPEN

A nanofabricated, monolithic, path-separated electron interferometer

Received: 19 December 2016
Accepted: 28 March 2017
Published online: 10 May 2017

Akshay Agarwal[1], Chung-Soo Kim[1], Richard Hobbs[1], Dirk van Dyck[2] & Karl K. Berggren[1]

Progress in nanofabrication technology has enabled the development of numerous electron optic elements for enhancing image contrast and manipulating electron wave functions. Here, we describe a modular, self-aligned, amplitude-division electron interferometer in a conventional transmission electron microscope. The interferometer consists of two 45-nm-thick silicon layers separated by 20 μm. This interferometer is fabricated from a single-crystal silicon cantilever on a transmission electron microscope grid by gallium focused-ion-beam milling. Using this interferometer, we obtain interference fringes in a Mach-Zehnder geometry in an unmodified 200 kV transmission electron microscope. The fringes have a period of 0.32 nm, which corresponds to the [111] lattice planes of silicon, and a maximum contrast of 15%. We use convergent-beam electron diffraction to quantify grating alignment and coherence. This design can potentially be scaled to millimeter-scale, and used in electron holography. It could also be applied to perform fundamental physics experiments, such as interaction-free measurement with electrons.

Electron interferometers have been used in many applications such as demonstration of double-slit interference[1] and the Ahronov-Bohm effect[2], exit-wave reconstruction[3], and imaging magnetotactic bacteria[4]. Most of these applications were made possible by Möllenstedt and Düker's invention of the electron biprism in 1956[5], which enabled wavefront-division interferometry in the electron microscope. This type of interferometry is fundamentally limited by the requirement of a highly coherent, field-emission electron source[6]; thermionic emission sources (such as LaB_6 and tungsten) lead to poor visibility of interference fringes from wavefront-division interferometry. This limitation also applies to the recently demonstrated double-slit electron interferometers[7–12] that used focused-ion-beam (FIB) fabricated slits. A second issue is that the integration of a biprism into a microscope requires considerable modification of the electron optical column.

The limitations of wavefront-division interferometry can potentially be overcome with an amplitude-division interferometer. Such an interferometer can provide much better interference fringe visibility (at the cost of reduced resolution[13]) with low-coherence electron sources and is hence very useful for applications where the sensitivity of the measurement is important. An amplitude-division interferometer for electrons was first proposed and demonstrated by Marton and co-workers[14–16]. This interferometer used three 10 nm thick, polycrystalline, epitaxially grown copper membranes that acted as diffraction gratings to split and recombine the electron beam. Multilayer interferometers using two layers at the edges of silicon crystals were later used by Dowell and Goodman[17,18], Buxton[19], Rackham[20], and Zhou[21,22]. Designs by Matteucci[23,24] raised the possibility of high-resolution interferometry with a thermionic source, and Ru[13,25] demonstrated interferometry without significant modification the electron column optics. A combination of crystalline gratings and biprisms was also employed in interferometry and holography setups by Herring[26,27], and Mertens[28]. Besides crystalline gratings, electron diffraction from nanofabricated gratings[29] has also been used in amplitude-division interferometry. For example, Gronniger *et al.*[30,31] and Bach *et al.*[32] constructed Mach-Zehnder and Talbot-Lau electron interferometers with thermionic electron guns, using three large-area gratings fabricated by optical interference lithography.

Despite these advances, amplitude-division electron interferometers have not been widely adopted. This lack of utilization is primarily due to the stringent requirements of positioning and orientation for precise alignment of the interferometer, which have resulted in considerable modification of the electron column in previous efforts, just as

[1]Department of Electrical Engineering and Computer Science, Massachusetts Institute of Technology, Cambridge, MA, USA. [2]EMAT, University of Antwerp, Groenenborgerlaan 171 2020, Antwerp, Belgium. Akshay Agarwal and Chung-Soo Kim contributed equally to this work. Correspondence and requests for materials should be addressed to K.K.B. (email: berggren@mit.edu)

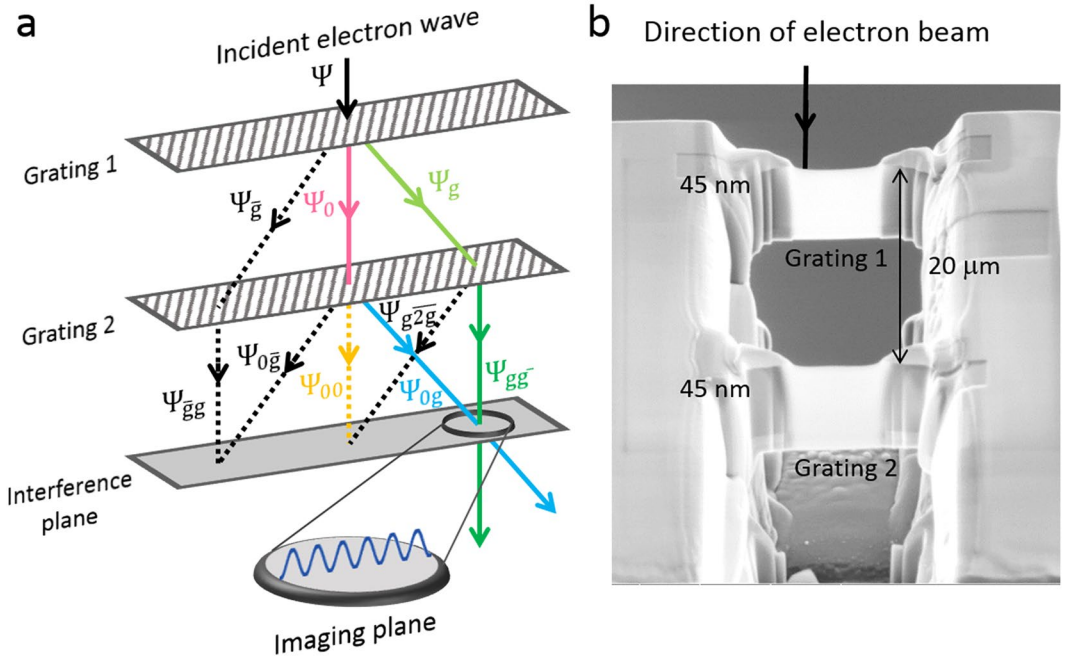

Figure 1. Two-grating electron interferometer. (**a**) Schematic of diffraction with 1-D gratings. The incident wave $\boldsymbol{\Psi}$ is diffracted into zero ($\boldsymbol{\Psi}_0$) and first ($\boldsymbol{\Psi}_g$ and $\Psi_{\bar{g}}$) order beams by grating 1, each of which diffracts again from grating 2. Any two diffracted partial waves with $\Delta\mathbf{g}_{net} = \mathbf{g}$ (see text for definition), such as $\boldsymbol{\Psi}_{0g}$ and $\boldsymbol{\Psi}_{g\bar{g}}$ interfere in the 'interference plane', thereby imaging the lattice planes corresponding to **g** onto this plane. We placed a CCD camera conjugate to the interference plane to capture the interference pattern. (**b**) Scanning electron micrograph of two-grating interferometer with $20 \pm 0.1\,\mu$m gap between the gratings. The thickness of each grating is 45 ± 5 nm. This image was taken at a 52° tilt at an electron energy of 5 keV and working distance of 4 mm.

for the biprism. For example, Marton[16] had to develop a mechanical manipulator to control translation and rotation of each grating for alignment. Gronniger's experiment[31] incorporated a laser interferometer to rotationally align the gratings to an accuracy of 1 mrad. Buxton and Zhou's double crystal interferometer overcame the requirement of alignment by using two silicon layers from the same crystal. However, it had limited applicability due to the small (~1 μm) gap between the crystals which made separation of interferometer paths difficult[33]. Complete path separation is important to ensure that one of the beams can be manipulated without affecting the other.

In this work, we fabricated a self-aligned electron interferometer using FIB sculpting of a thick single crystal of silicon (110). We also demonstrated interferometry in the Mach-Zehnder configuration by directly imaging the interference between two electron beams diffracted from the gratings in a transmission electron microscope (TEM). The interferometer was integrated in the TEM with no modification of the electron column. Diffraction and interference experiments confirmed that our grating architecture was aligned to an accuracy of 220 μrad.

Figure 1(a) schematically depicts diffraction from the two-grating interferometer. To simplify the description we use a 1-D grating with lattice constant a and depict only the zeroth and first order diffracted waves from each grating. D denotes the gap between the two gratings. Solid lines represent the waves of interest in the interferometer. We use Zhou's notation[22] to denote the diffracted waves from the two gratings. The first grating splits the incident wave $\boldsymbol{\Psi}$ into the zero ($\boldsymbol{\Psi}_0$, pink) and first order ($\boldsymbol{\Psi}_g$, light green and $\boldsymbol{\Psi}_{\bar{g}}$, black) diffracted partial waves. Here $|\mathbf{g}| = 2\pi/a$ is the magnitude of the 1-D reciprocal lattice vector. Each of these waves is incident at a Bragg angle on the second grating and gets diffracted again, provided the two gratings are mutually aligned. The re-diffracted partial waves arising from $\boldsymbol{\Psi}_0$ are $\boldsymbol{\Psi}_{00}$ (yellow), $\boldsymbol{\Psi}_{0g}$ (blue), and $\boldsymbol{\Psi}_{0\bar{g}}$ (black), and similarly for $\boldsymbol{\Psi}_g$ ($\boldsymbol{\Psi}_{g0}$ (light green), $\boldsymbol{\Psi}_{g\bar{g}}$ (dark green)) and $\boldsymbol{\Psi}_{\bar{g}}$ ($\boldsymbol{\Psi}_{\bar{g}0}$ and $\boldsymbol{\Psi}_{\bar{g}g}$, both black). Defining $\mathbf{g}_{net}$ as the sum of the subscript **g**-vectors for each wave, we see that any two diffracted waves $\boldsymbol{\Psi}_{g1g2}$ and $\boldsymbol{\Psi}_{g3g4}$ for which $|\Delta\mathbf{g}_{net}| = |(\mathbf{g3} + \mathbf{g4}) - (\mathbf{g1} + \mathbf{g2})| = 0$, such as $\boldsymbol{\Psi}_{g\bar{g}}$ and $\boldsymbol{\Psi}_{00}$, or $\boldsymbol{\Psi}_{0g}$ and $\boldsymbol{\Psi}_{g0}$, emerge parallel to each other after diffraction from both gratings. Waves with $|\Delta\mathbf{g}_{net}| = \mathbf{g}$ such as $\boldsymbol{\Psi}_{0g}$ and $\boldsymbol{\Psi}_{g\bar{g}}$ overlap and interfere with each other. This interference occurs in a plane parallel to the two gratings and located D units below the second grating. We will henceforth refer to this plane as the 'interference plane'. In our experiments, we used $\boldsymbol{\Psi}_{0g}$ and $\boldsymbol{\Psi}_{g\bar{g}}$ to construct a separate-path interferometer in the TEM. An equivalent interferometer is formed by $\boldsymbol{\Psi}_{\bar{g}g}$ and $\boldsymbol{\Psi}_{0\bar{g}}$. The interference fringes can be read out by placing a third grating in the interference plane and recording the electron counts on an integrating detector positioned in the path of either of the output waves ($\boldsymbol{\Psi}_{0g}$ and $\boldsymbol{\Psi}_{g\bar{g}}$). Translation of the third grating perpendicular to the optical axis leads to oscillations in these counts due to change in the relative phase between the two interfering waves. Working in a TEM allowed us to observe interference fringes by directly imaging the interference plane, which precluded the need for a third grating.

Experiment

Figure 1(b) shows the fabricated two-grating structure that we used for interference experiments. As described in Methods, we fabricated our gratings on a workpiece consisting of single-crystalline silicon cantilevers suspended from a tungsten support grid using FIB milling (FEI Helios Nanolab 600 and 650). The grid could be inserted into a regular TEM sample holder. The gap between the gratings is $20 \pm 0.1\,\mu$m, where $0.1\,\mu$m reflects the precision with which we could position the gratings. The thickness of each grating was 45 ± 5 nm. This thickness was obtained by averaging over several measurements at the edge of the grating; 5 nm was the maximum variation in these measurements. We aimed to minimize the thickness of each grating, to suppress decoherence due to inelastic scattering. However, large area gratings thinner than about 40 nm were found to bend, thereby introducing misalignment in the interferometer. Another two-grating structure with $2.5\,\mu$m gap between the gratings was used to characterize the alignment and coherence of diffracted beams, as described later. The grid was mounted into the sample stage of a TEM (JEOL 2010F) for electron diffraction and interferometry experiments. These experiments were performed at an electron energy of 200 keV.

As discussed previously, separating the paths of the interfering beams is critical to independently manipulating the phase of each beam. In order to determine the beam diameter, semi-angle of convergence α, and grating separation for a separate path interferometer, we simulated the diffraction of 200 keV electrons from two gratings using the Gaussian-Schell model (GSM)[34–36]. GSM assumes that the incident beam consists of a distribution of independent Gaussian modes and allows for the description of partially coherent beams using the mathematics of Gaussian beams. We used McMorran and Cronin's results on the diffraction of a GSM beam from two gratings[36], with a beam spatial coherence length equal to 20% of the beam diameter, in our simulations. This estimate of the spatial coherence was based on theoretical calculations for small condenser apertures[37,38], and supported by preliminary experiments (described in Discussion) to characterize the beam coherence. We assumed that the degree of temporal coherence of the beam was close to 1, and hence ignored the effects of partial temporal coherence in our simulations[39]. We used the (000) and $(\bar{1}\bar{1}1)$ diffracted beams of silicon to design our interferometer. Therefore, each grating in the simulation was one-dimensional with a period of 0.32 nm, which is equal to the period of the $[\bar{1}\bar{1}1]$ lattice planes. An important *caveat* here is that the gratings in our simulation were amplitude gratings, while thin layers of silicon behave as phase gratings at the electron energies used in the TEM. However, this difference did not affect the diffraction angles, and hence the set of parameters that allowed the beams to separate, which was the primary focus of the simulations. We chose a beam diameter of 240 nm at the first grating and $\alpha = 4$ mrad, with beam crossover (*i.e.*, beam focus) between the second grating and interference plane. With these parameters, the beam diameter in the the interference plane was 80 nm. The chosen parameters prevented overlap between the diffracted beams $\mathbf{\Psi_0}$ and $\mathbf{\Psi_g}$ on the second grating, and $\mathbf{\Psi_{00}}$ and $\mathbf{\Psi_{g\bar{g}}}$ at the interference plane, and thus ensured complete path separation. The choice of beam parameters was dictated by experimental considerations, as explained in the supplementary information.

Figure 2(a) shows the simulated diffraction of a GSM beam with these parameters from two 0.32 nm-period gratings separated by $20\,\mu$m. The simulation included diffracted beams up to second order. For the following simulation and experimental results in this section, $\mathbf{g} = (\bar{1}\bar{1}1)$. As described earlier, any two diffracted beams with $|\Delta\mathbf{g}_{\text{net}}| = \mathbf{g}$ overlap in the interference plane, which for our interferometer was $20\,\mu$m below the second grating. In Fig. 2(b), we magnify the region around the interference plane to see the overlapping beams. Note that the variation in fringe contrast in this image was caused by undersampling and consequent aliasing of the underlying lattice-spaced interference pattern in the simulation. However, the extent of these aliased fringes along the optical axis, $\Delta z \approx 2.7\,\mu$m, was the same as that of the actual interference fringes. Δz is proportional to the spatial coherence of the beams, as discussed later. Figure 2(c) shows a cross-section of the overlapping beams in the interference plane with further magnification and finer meshing; we obtained fringes with the period of the corresponding lattice, *i.e.*, 0.32 nm.

In Fig. 2(d), we show experimental demonstration of this interferometer in the Mach-Zehnder geometry. Note that we focused the electron beams very close to the image planes, to obtain the images in this figure and make the movement of various beams easier to follow. However, to get high-resolution lattice/interference fringe images, we defocused the beams to the designed diameter and α.

In order to see the various beams diffracted by the two gratings, we translated the interferometer vertically by changing the TEM stage height z. This procedure enabled us to successively image planes between second grating and interference plane, and thus follow the evolution of the diffracted beams in these planes. We started our experiment with the second (lower) grating in the eucentric plane. In Fig. 2(d), we denote the stage height here as $z_1 = 0\,\mu$m. At this height, we imaged the primary and first-order diffracted beams ($\mathbf{\Psi_0}$ and $\mathbf{\Psi_g}$, circled in pink and light green, respectively) on this grating. The separation s between $\mathbf{\Psi_0}$ and $\mathbf{\Psi_g}$ was 160 nm as expected for $D = 20\,\mu$m ($s = 2\theta_B D$ where $2\theta_B \simeq \lambda_{\text{electron}}/a$). As seen in Fig. 2(e), upon underfocusing the beams to the designed beam diameter (80 nm) at the second grating and imaging $\mathbf{\Psi_0}$ at high-resolution, we obtained a lattice-resolved image of the crystalline silicon. We then translated the stage to $z_2 = 2\,\mu$m below the second grating, to image the beams diffracted by this grating. $\mathbf{\Psi_{0g}}$ (circled in blue) was visible at a distance of 15 nm from $\mathbf{\Psi_{00}}$. $\mathbf{\Psi_{g\bar{g}}}$ (circled in dark green) was at a distance of 160 nm from $\mathbf{\Psi_{00}}$. $z_3 = 5.5\,\mu$m below the second grating, the distance between $\mathbf{\Psi_{0g}}$ and $\mathbf{\Psi_{00}}$ increased to 42 nm. $\mathbf{\Psi_{g\bar{g}}}$ (circled in dark green) remained 160 nm away from $\mathbf{\Psi_{00}}$. $\mathbf{\Psi_{g2\bar{g}}}$ (not circled) was also visible between $\mathbf{\Psi_{0g}}$ and $\mathbf{\Psi_{g\bar{g}}}$. On moving $z_4 = 10.5$ and $z_5 = 16\,\mu$m below the second grating, we observed that $\mathbf{\Psi_{0g}}$ continued moving away from $\mathbf{\Psi_{00}}$ and towards $\mathbf{\Psi_{g\bar{g}}}$. The distance between $\mathbf{\Psi_{0g}}$ and $\mathbf{\Psi_{g\bar{g}}}$ was 78 and 29 nm for z_4 and z_5 respectively. Finally, when we reached $z_6 = 20\,\mu$m below the second grating, $\mathbf{\Psi_{0g}}$ and $\mathbf{\Psi_{g\bar{g}}}$ overlapped completely; the CCD camera was now conjugate to the interference plane. As shown in Fig. 2(f), we observed interference fringes with a period of 0.32 nm within the overlap spot. We took this image by overfocusing the beam to a diameter of 80 nm, so that the beam diameter and α were at their designed values. Since the fringe

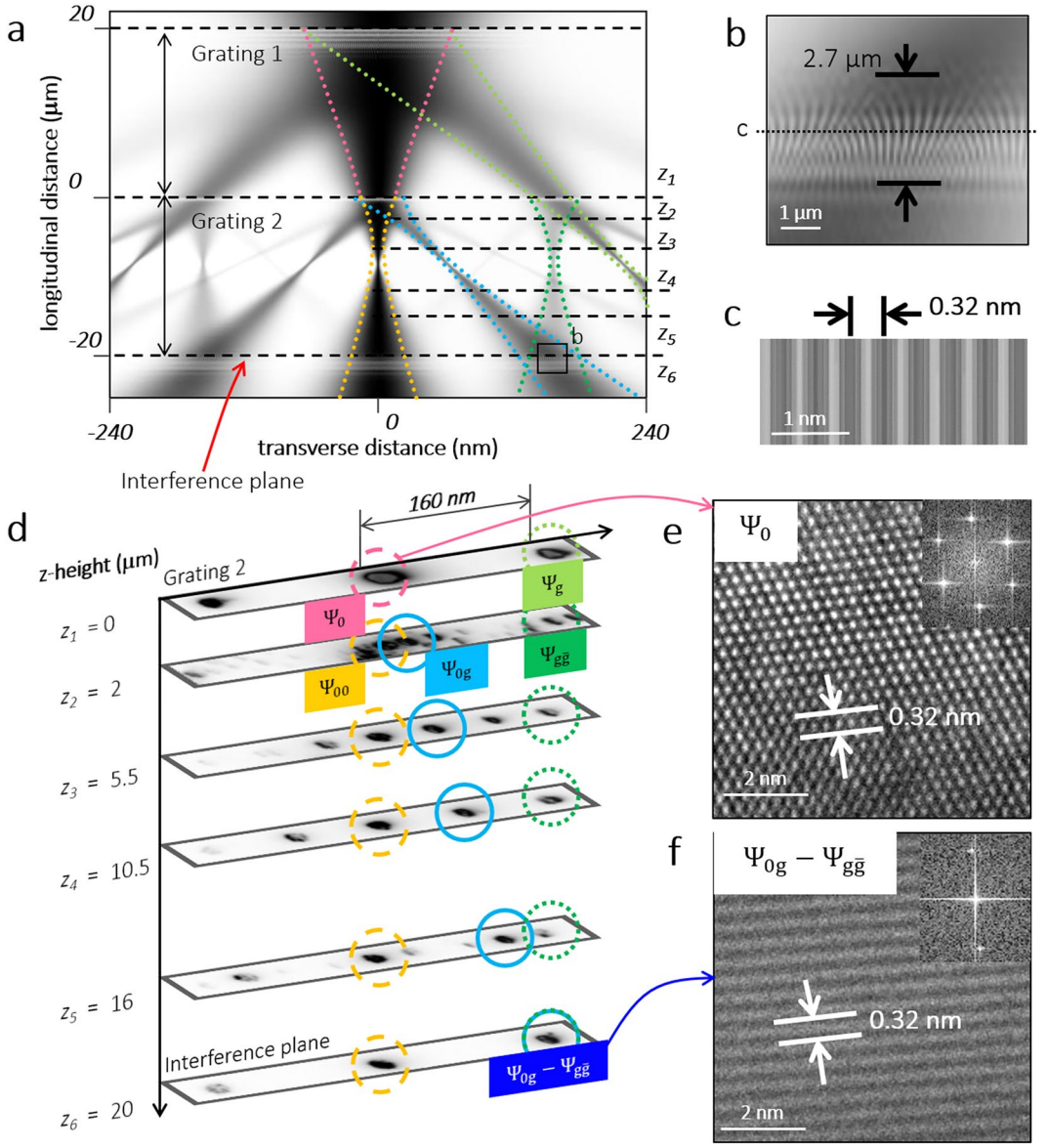

Figure 2. Electron interferometry with the two-grating structure. (**a**) GSM simulation of diffraction from the 20 μm interferometer. The black dashed lines represent imaging planes at different stage heights z, as explained in the text. In the interference plane, the two beams Ψ_{0g} (blue) and $\Psi_{g\bar{g}}$ (dark green) overlap. (**b**) Magnified view of the region around the interference plane as indicated in (a). For a spatial coherence length equal to 20% of the beam diameter, the interference fringes extend for $\Delta z \approx 2.7\,\mu m$ along the optical axis. The contrast seen in this image is caused by undersampling of the actual interference fringes, as explained in the text. (**c**) Magnified cross-section of the overlapping beams at the interference plane, as indicated in (**b**), showing fringes with the periodicity of the $[\bar{1}\bar{1}1]$ planes, 0.32 nm. (**d**) ($z_1 = 0$) Ψ_0 (center, pink circle), Ψ_g (right, light green circle) and $\Psi_{\bar{g}}$ (left) diffracted beams on the second grating. ($z_2 = -2\,\mu m$) Ψ_{0g} (circled in blue) separates out from Ψ_{00} (circled in yellow). $\Psi_{g\bar{g}}$ is circled in dark green on the right. ($z_3 = -5.5\,\mu m$, $z_4 = -10.5\,\mu m$ and $z_5 = -16\,\mu m$) Ψ_{0g} moves towards $\Psi_{g\bar{g}}$. The measured distances between the beams are included in the text. ($z_6 = -20\,\mu m$) The two beams Ψ_{0g} and $\Psi_{g\bar{g}}$ overlap and interfere. (**e**) TEM micrograph of the lattice of the second grating from the Ψ_0 beam at $z_1 = 0$. Inset shows the Fourier transform of the image, with multiple spots corresponding to the different lattice planes of silicon (110). (**f**) TEM micrograph of fringes from the interference of Ψ_{0g} and $\Psi_{g\bar{g}}$ beams at $z_6 = -20\,\mu m$ with a period 0.32 nm. The inset shows the Fourier transform of the image. Only one set of points (corresponding to $\mathbf{g} = (\bar{1}\bar{1}1)$) are seen around the central spot, confirming the origin of the fringes.

contrast was quite low (<20%), we used the Fourier transform of the live image (inset, Fig. 2(f)) to monitor the appearance of the fringes. The presence of a single set of spots in the Fourier transform (corresponding to $\mathbf{g} = (\bar{1}\bar{1}1)$) confirmed that these fringes were formed due to the interference between Ψ_{0g} and $\Psi_{g\bar{g}}$.

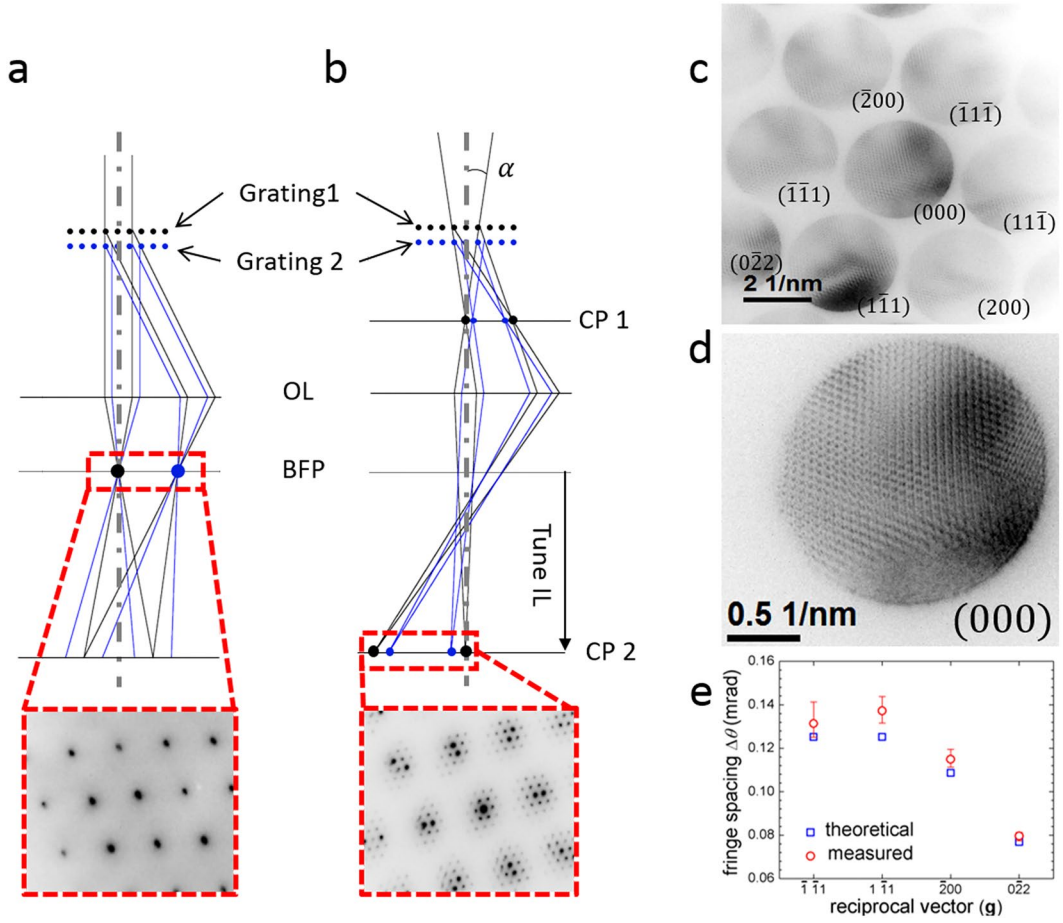

Figure 3. Parallel and convergent-beam from the two-grating structure. (**a**) Ray diagram for a nearly parallel incident beam (small α). Diffracted beams with $\Delta\mathbf{g}_{\mathbf{net}}$(see text for explanation) = 0 are focused to the same point in the back-focal plane (BFP) of the objective lens (OL). Thus the diffraction pattern is the same as single-layer silicon as seen in the experimentally obtained SADP (red box). The experimental SADP is for $\alpha = 0.2$ mrad. (**b**) Ray diagram for a convergent incident beam (large α). The spots in the BFP broaden to disks formed by overlap between waves with $\Delta\mathbf{g}_{\mathbf{net}} = 0$ which leads to interference fringes within each spot. At the first and second crossover plane (CP 1 and CP 2 respectively), these beams focus at horizontally displaced points due to the gap between the gratings. The red box is the experimental diffraction pattern in CP 2 with $\alpha = 4$ mrad, showing multiple closely spaced spots due to this horizontal displacement. (**c**) BFP diffraction pattern with $\alpha = 4$ mrad showing interference fringes for the 2.5 μm-gap sample. The $\mathbf{g}_{\mathbf{net}}$ corresponding to each spot is indicated. (**d**) Magnified view of the $\mathbf{g}_{\mathbf{net}} = (000)$ spot showing interference fringes (**e**) Angular separation of fringes in the (000) spot, *i.e.*, formed by interference between diffraction orders with $\mathbf{g}_{\mathbf{net}} = 0$. In this case, the **g**-vectors from the two gratings must be equal in magnitude and oppositely directed. These vectors are indicated on the *x*-axis.

Discussion

Successful demonstration of interference was critically dependent on the alignment between the two gratings. Further, the diffracted beams from each grating had to be sufficiently coherent to form visible fringes upon interference. Therefore, before performing electron interferometry experiments with the 20 μm interferometer, we checked the alignment of our two-grating structures and the coherence of the diffracted beams by using parallel and convergent electron diffraction through a 2.5 μm-gap structure. We also performed these tests for the 20 μm-gap structure, as reported in the supplementary information. Although the tests indicated that the 20 μm-gap structure was well-aligned, the convergent beam diffraction results were difficult to interpret due to limitations of our TEM. We discuss these limitations in detail later.

For testing alignment, we took a selected area diffraction pattern (SADP) with a wide, nearly parallel electron beam ($\alpha = 0.2$ mrad); Fig. 3(a) shows a ray diagram for this situation. After diffraction from the two gratings, waves with a common value of $\mathbf{g}_{\mathrm{net}}$, *i.e.*, with $\Delta\mathbf{g}_{\mathrm{net}} = 0$ should be parallel to each other. Therefore, we expect these waves to be focused at the same point at the back focal plane (BFP) of the TEM objective lens. Hence, the focused SADP should be the same as for single-layer silicon, provided the two gratings are well-aligned. This prediction was confirmed in the experimentally observed SADP, as shown in the box at the bottom of Fig. 3(a). We did not observe any displacement between the focused diffraction spots from the two gratings for camera lengths up to 200 cm.

For testing coherence between beams diffracted from the two gratings, we increased α to 4 mrad; in Fig. 3(b) we depict the ray diagram for electron diffraction with a convergent beam. As a result of the beam convergence, the focused spots in the BFP broadened into disks, with each disk formed by overlap between beams with $\Delta\mathbf{g}_{\text{net}} = 0$. We focused the diffraction pattern by tuning the intermediate lens (IL) current. This change in the IL current changed the plane being imaged from the BFP to the second 'crossover plane' (CP 2), which was an image of the focused beams at the first crossover plane (CP 1) below the two gratings. In this plane, the gap between the two gratings led to horizontal displacement between the focused spots from beams with $\Delta\mathbf{g}_{\text{net}} = 0$[40]. The box at the bottom of Fig. 3(b) shows the experimental SADP with for $\alpha = 4$ mrad. This SADP is reminiscent of a Moiré pattern, except that the extra diffraction spots were created not due to different lattice constants[41], but rather due to the gap between the gratings. Note that this displacement was unrelated to the misalignment-induced displacement at the BFP expected for a parallel beam. The supplementary information contains an extended discussion of convergent beam diffraction from the two-grating structures, along with supporting experiments to verify the mechanism outlined above.

Within each spot in the BFP, we observed interference fringes with multiple orientations and periods, as seen in the SADP in Fig. 3(c). We will henceforth refer to these fringes as '**BFP** fringes' to differentiate them from the imaging plane fringes obtained with the 20 μm interferometer. Interference between $\mathbf{\Psi_{00}}$, $\mathbf{\Psi_{gg}}$ and $\mathbf{\Psi_{\bar{g}\bar{g}}}$ led to BFP fringes within the zero-order spot (since $\mathbf{g}_{\text{net}} = 0$ for each of these beams) perpendicular to $\mathbf{g}$, as seen in Fig. 3(d). Similarly, interference between $\mathbf{\Psi_{0\bar{g}}}$ and $\mathbf{\Psi_{g2\bar{g}}}$ resulted in BFP fringes in the $\mathbf{g}_{\text{net}} = \bar{\mathbf{g}}$ spot. Inclusion of all the silicon reciprocal lattice vectors in this description would lead to the different interference fringe orientations and periods in Fig. 3(c,d). These BFP fringes confirmed that the beams diffracted from the first and second gratings were at least partially coherent with each other. In previous work by Buxton and Zhou, the angular separation between these fringes was estimated to be $\Delta\theta \sim a/D$[19,21,22]. Physically, a larger reciprocal lattice vector and/or gap between the gratings increases the angle of intersection between the overlapping beams in the BFP, thus reducing the period of the resulting fringes. Importantly, Buxton and Zhou's estimate for $\Delta\theta$ does not depend on α. We measured $\Delta\theta$ for $\alpha = 4$, 2, 0.9, and 0.5 mrad, by varying the size of the selected-area diffraction (SAD) aperture, keeping all lens currents constant. In Fig. 3(e), we compare the mean of $\Delta\theta$ for these values of α with Buxton and Zhou's estimate. For fringes within the zero order spot, with $\mathbf{g} = (\bar{1}\,\bar{1}1)$, $(1\bar{1}1)$, $(\bar{2}00)$ and $(0\bar{2}2)$, the experimental values agreed with the estimate to an accuracy of 5%, 9.6%, 5.7% and 3.7% for the four values of $\mathbf{g}$, respectively. The variation in the difference between the experimental values and the estimate was due to residual astigmatism in the imaging system. The change in $\Delta\theta$ with α was smaller than 3% of the mean for all orientations of $\mathbf{g}$. Thus, the chief source of error in $\Delta\theta$ was the pixel size of our CCD detector. The error bars for each value of $\mathbf{g}$ in Fig. 3(e) indicate the range of $\Delta\theta$ with an error of one pixel. Further, the contrast of the BFP fringes increased from 15% (for $\alpha = 4$ mrad) to 33% (for $\alpha = 0.5$ mrad). As noted earlier, we expected the degree of temporal coherence to be close to 1. Hence, the fringe contrast can be used as an estimate of the degree of spatial coherence of the diffracted beams[3] for different SAD apertures. In the GSM interference simulations, we used a slightly higher value of the degree of spatial coherence (20%) than that measured here (15%) for $\alpha = 4$ mrad, because of contrast reduction due to unequal amplitudes of the interfering beams. We elaborate on this point later.

We obtained similar SADP from the 20 μm-gap-structure with parallel and convergent beams, as discussed in the supplementary information. The BFP fringe period was expected to be ~10 times smaller than that for the 2.5 μm gap sample, which was very close to the resolution limit of the CCD detector of our TEM. We were thus unable to image the BFP fringes with the 20 μm-gap-structure. While obtaining the imaging plane fringes with this structure, as described earlier, we noted a slight displacement between the focused spots from each wave, from which we estimated a misalignment of ~220 μrad between the two gratings. A detailed discussion of this measurement is provided in the Supplementary Information. We analyze possible causes for this misalignment later. However, note that this misalignment was an order of magnitude lower than both the maximum tolerance for Marton's interferometer (1.2 mrad)[16,42] and the misalignment for Gronniger's interferometer (1 mrad)[31]. Also, as noted earlier, we were able to position each grating with an accuracy of $\Delta D = 100$ nm. The fractional error in positioning of the gratings $\Delta D/D = 0.005$ was greater than Marton's tolerance specifications ($\Delta D/D = 0.004$) and a factor of ~6 larger than the corresponding value for Gronniger. More careful fabrication should allow us to position our gratings with better accuracy.

We again stress that the BFP fringes obtained here are different in origin from the imaging plane fringes reported with the 20 μm interferometer. In the former case, beams with $\Delta\mathbf{g}_{\text{net}} = 0$ interfere in the BFP due to focusing by the objective lens, while in the latter case, beams with $\Delta\mathbf{g}_{\text{net}} = \mathbf{g}$ interfere due to diffraction from the second grating. Although the BFP fringes are useful for characterizing the coherence of the diffracted beams, the small gap results in the beams not being fully separated on the second grating. Hence this structure cannot be used in experiments that require the placement of a sample in the path of one of the beams, *i.e.*, as a path-separated interferometer.

We now return to the imaging plane fringes with the 20 μm interferometer. The observed fringe spacing of 0.32 nm would have also been produced by Talbot self-imaging[43,44]. However, the separation between the two gratings was ~250 times the Talbot length z_T for the $(\bar{1}\,\bar{1}1)$ lattice planes of silicon ($z_T = 2a^2/\lambda_{\text{electron}} = 82$ nm for 200 keV electrons), which made Talbot fringes unlikely. A Moiré deflectometer[45] would have also produced fringes of the same period. The direct imaging method employed here, which showed the separation and overlap of diffracted beams, along with our measurement of beam coherence, made this explanation unlikely too. Thus, the observed fringes could be attributed to coherent overlap between the diffracted beams in a Mach-Zehnder geometry.

The fringe images were captured with an exposure time between 1 and 5 seconds. Longer exposures lead to blurring due to mechanical vibrations in the sample stage, while shorter exposures result in poor signal-to-noise ratio.

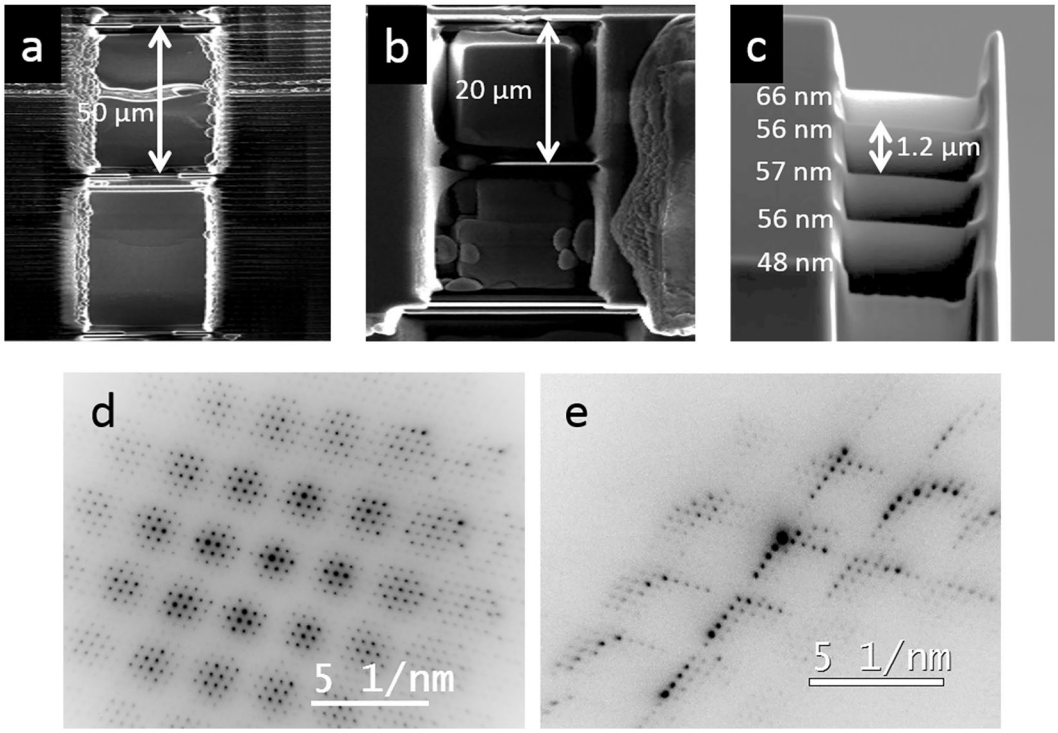

Figure 4. Controlling the geometry of the grating interferometers. Side-view SEM micrographs of three-grating structure with (**a**) 50 and (**b**) 20 µm gap between the gratings, showing control over the gap and lateral area of each grating respectively. (**c**) 52°-tilt SEM micrograph of five grating structure with 1.2 µm gap between the gratings, showing control over the number of gratings. The mean thickness of each grating is indicated. (**d**) Convergent-beam diffraction pattern from structure in (**b**). (**e**) Convergent-beam diffraction pattern from structure in (**c**).

The spatial coherence length of the electron beam can be interpreted as the diameter of a disk of points, around any given point in the beam, that have a fixed mutual phase relationship. The wider this disk, the greater the extent of coherent interference along the optical axis. This increases Δz, the distance along the optical axis over which the fringes persist. In our experiment, $\Delta z \sim 3\,\mu m$. This value is close to the estimate of 2.7 µm from our simulations, as shown in Fig. 2(b), which further supports our assumption of the spatial coherence length of the beam in the simulation.

The maximum fringe contrast observed was 15%, similar to the contrast for the BFP fringes with $\alpha = 4$ mrad described earlier. For two interfering beams of equal amplitude, the fringe contrast is ideally equal to the degree of coherence. However, as can be seen from the images at z_4 and z_5 in Fig. 2(d), the intensities of the $\mathbf{\Psi_{0g}}$ and $\mathbf{\Psi_{gg}}$ beams were quite different. The ratio of the average intensity of the two beams from the image at z_4 was 0.38. This difference in intensity reduced the fringe contrast by a factor of ~0.9 from its ideal value. Tilting to the two-beam condition is a possible solution to enhancing the intensities of the interfering beams and thus improving contrast; however, the slight misalignment between the two gratings noted earlier was sufficient to prevent us from achieving the two-beam condition simultaneously for both crystals. As discussed in the Supplementary Information, we expect this to be rotational misalignment between the gratings. Other sources of misalignment include bending of the crystals during fabrication, and the rotation of the electrons in the pre-field of the objective lens, in which the sample is immersed.

Due to bending and variations in thickness in each of the two gratings, the relative intensities of the diffracted beams varied with translation in the plane of the gratings (the *x*-*y* plane). Since translation along the optical axis (*z*) led to small translations in the *x*-*y* plane too, the intensities of the beams changed as we moved from the plane of the second grating to the overlap plane. This can be seen in the reduction of the intensity of the $\mathbf{\Psi_{\bar{g}}}$ spot between the images at z_1 and z_2 in Fig. 2(d).

This interferometer design can easily be scaled to larger gaps and numbers of gratings, which would facilitate its use in potential interferometry and holography setups by simplifying the placement of a sample and application of a field differential between the two beams. Figure 4(a) shows a fabricated structure with 50 µm gap between the gratings. We are currently limited in expanding this gap further by the thickness of commercially available TEM grids. Figure 4(b) shows a three-grating structure with different lateral area of each grating, which allowed us to study diffraction through one, two or three gratings separately. Figure 4(c) shows a five-grating structure with 1.2 µm gap between the gratings, demonstrating control over the number of gratings in the fabricated structures. Figure 4(d,e) show convergent beam diffraction from the grating structures in Fig. 4(b,c) respectively, again showing multiple closely-spaced spots, as discussed for the two-grating structure.

Although we fabricated a three-grating interferometer (as shown in Fig. 4(c)) to attempt a Marton-type experiment[16], the interpretation of this experiment was hindered by contrast fluctuations. These fluctuations were again caused by bending and thickness variation in each grating. In addition to interference effects, the intensity of each diffracted beam was also affected by the thickness of each grating. The difficulty in determining the exact thickness at every point of each grating made it challenging to separate this effect from the interference effects. This issue could be addressed by fabricating very thin (~10 nm) gratings to suppress dynamical diffraction effects. In the two-grating results described earlier, this problem was circumvented by effectively replacing the third grating with a screen on which the interference was imaged directly.

Conclusion

We have fabricated a monolithic, two-grating electron interferometer, which showed a misalignment of ~220 μrad. This misalignment was an order of magnitude lower than that of similar designs reported previously. We demonstrated a path-separated electron interferometer in the Mach-Zehnder geometry, and obtained interference fringes with a period of 0.32 nm. The fringe contrast was used to determine the spatial coherence of the TEM electron beam to be ~20%.

This interferometer design is self-aligned, configurable, scalable to larger dimensions, and continues progress towards electron interferometry and holography in a conventional TEM with no modification of the optical column or sample holder[13,23]. The use of this interferometer with a thermionic emission gun will be an area of future work. The interferometer could also be incorporated into a specially-designed electron-optic column for specific applications. The separation of paths on the second grating makes it feasible to place an absorbing object in the path of one of the beams, which may allow the implementation, with electrons, of Elitzur and Vaidman's scheme for interaction-free imaging[46,47]. In the same vein, we can also configure the gratings in order to implement multiple and repeated quantum interrogation of distinct absorbing objects[48,49]. An important requirement for such structures is that the error in positioning of each grating (~100 nm as noted earlier) be smaller than Δz, to ensure coherent interference on each grating. This requirement is met by our design. A major challenge that will need to be addressed is the bending and variations in thickness of each grating, which would make interpretation of any which-path experiment difficult. Although these variations were small enough to still allow visible interference fringes, future quantitative work will require their minimization. In the final stage of review, we became aware of recently published work by Tavabi *et al.*[50] on FIB-fabricated silicon crystal grating interferometers. In this work, crystal grating interferometers with a gap of upto 8 μm were studied, and the resulting interference fringes correspond to the results reported here in Fig. 3.

Methods

FIB Fabrication. We fabricated the two-grating interferometers by gallium FIB milling (FEI Helios Nanolab 600 and 650) of single-crystal silicon (110) cantilevers on tungsten TEM grids (Nanomesh, from Hitachi High-Tech). The gratings were made on one monolithic silicon (110) crystal cantilever with two thicknesses (5 and 40 μm). Figure S1 in the supplementary information summarizes the steps in our fabrication process. We initially placed the cantilever perpendicular to the ion-beam optical axis. The first step was milling of windows through the 5/40 μm thick silicon cantilevers using 30 kV gallium ion beam. These windows defined the lateral extent of the gratings. They also acted as a milling stopper, and helped to reduce material re-deposition and secondary sputtering in subsequent steps. We then placed the cantilever along the direction of the optical axis and deposited two 3 μm thick platinum layers to define the gratings, and protect them from ion-beam damage. Next we milled the unprotected silicon at 30 kV and 21 nA beam current. This step at large current and energy milled most of the silicon between the gratings. It was important here to leave substantial (~500 nm) thickness at each grating to allow for some beam focusing errors and resulting damage in the non-milled area. The gratings were then polished, first at successively lower currents (down to 50 pA) and then at lower energies (down to 2 kV) to give the final structure. The polishing step thinned down the gratings to $<$50 nm and removed most of the amorphous layer formed from ion-beam damage. The final polishing was done at a slight tilt (up to 5° in either direction) to improve the uniformity of thickness each grating. We restricted the lateral dimensions of each grating to be 10 μm by 10 μm to avoid bending of the membranes.

References

1. Merli, P. G., Missiroli, G. F. & Pozzi, G. On the statistical aspect of electron interference phenomena. *American Journal of Physics* **44**, 306–307 (1976).
2. Tonomura, A. *et al*. Evidence for aharonov-bohm effect with magnetic field completely shielded from electron wave. *Phys. Rev. Lett.* **56**, 792–795 (1986).
3. Lichte, H. & Lehmann, M. Electron Holography-basics and applications. *Reports on Progress in Physics* **71**, 016102 (2008).
4. Dunin-Borkowski, R. E. *et al*. Magnetic microstructure of magnetotactic bacteria by electron holography. *Science* **282**, 1868–1870 (1998).
5. Möllenstedt, G. & Düker, H. Beobachtungen und messungen an biprisma-interferenzen mit elektronenwellen. *Zeitschrift für Physik* **145**, 377 (1956).
6. Cowley, J. M. Twenty forms of electron holography. *Ultramicroscopy* **41**, 335–348 (1992).
7. Frabboni, S., Gazzadi, G. C. & Pozzi, G. Young's double-slit interference experiment with electrons. *American Journal of Physics* **75**, 1053–1055 (2007).
8. Frabboni, S., Gazzadi, G. C. & Pozzi, G. Nanofabrication and the realization of feynman's two-slit experiment. *Applied Physics Letters* **93** (2008).
9. Frabboni, S., Frigeri, C., Gazzadi, G. C. & Pozzi, G. Two and three slit electron interference and diffraction experiments. *American Journal of Physics* **79**, 615 (2011).
10. Frabboni, S. *et al*. The young-feynman two-slits experiment with single electrons: Build-up of the interference pattern and arrival-time distribution using a fast-readout pixel detector. *Ultramicroscopy* **116**, 73–76 (2012).
11. Frabboni, S., Gazzadi, G. C., Grillo, V. & Pozzi, G. Elastic and inelastic electrons in the double-slit experiment: A variant of Feynman's which-way set-up. *Ultramicroscopy* **154**, 49–56 (2015).

12. Bach, R., Pope, D., Liou, S.-H. & Batelaan, H. Controlled double-slit electron diffraction. *New Journal of Physics* **15**, 033018 (2013).
13. Ru, Q. Incoherent electron holography. *Journal of Applied Physics* **77**, 1421 (1995).
14. Marton, L. Electron interferometer. *Physical Review* **85**, 1057–1058 (1952).
15. Marton, L., Simpson, J. A. & Suddeth, J. A. Electron Beam Interferometer. *Physical Review* **90**, 490–491 (1953).
16. Marton, L., Simpson, J. A. & Suddeth, J. A. An Electron Interferometer. *Review of Scientific Instruments* **25**, 1099–1104 (1954).
17. Dowell, W. C. T. & Goodman, P. Image formation and contrast from a convergent electron beam. *Philosophical Magazine* **28**, 471–473 (1973).
18. Dowell, W. C. T. Electron interference in shadow microscopy. *Optik* **47**, 195–204 (1977).
19. Buxton, B. F., Rackham, G. M. & Steeds, J. The Dynamical Theory of a Double Crystal Interferometer. In *Ninth International Congress on Electron Microscopy, Toronto, Vol. 1*, 188–189 (1978).
20. Rackham, G. M., Loveluck, J. E. & Steeds, J. W. A double-crystal electron interferometer. *Electron Diffraction 1927–1977* ed. P. J. Dobson, J. B. Pendry and C. J. Humphreys (London, Bristol: The Institute of Physics) 435–440 (1977).
21. Zhou, F., Plies, E. & G., M. Double -crystal interferometer combined with CBED technique. *Optik* **98**, 95–100 (1995).
22. Zhou, F. The principle of a double crystal electron interferometer. *Journal of Electron Microscopy* **50**, 371–376 (2001).
23. Matteucci, G., Missiroli, G. F. & Pozzi, G. Amplitude Division Electron Interferometry. *Ultramicroscopy* **6**, 109–113 (1981).
24. Matteucci, G., Missiroli, G. F. & Pozzi, G. The Realization of Amplitude Division Electron Interferometry Demonstrated on Ferromagnetic Domain Walls. *Ultramicroscopy* **7**, 295–298 (1982).
25. Ru, Q., Osakabe, N., Endo, J. & Tonomura, A. Electron holography available in non-biprism transmisson electron microscope. *Ultramicroscopy* **53**, 1–7 (1994).
26. Herring, R. A., Pozzi, G., Tanji, T. & Tonomura, A. Realization of a mixed type of interferometry using convergent-beam electron diffraction and an electron biprism. *Ultramicroscopy* **50**, 94–100 (1993).
27. Herring, R. A., Pozzi, G., Tanji, T. & Tonomura, A. Interferometry using convergent electron diffracted beams plus an electron biprism (CBED+EBI). *Ultramicroscopy* **60**, 153–159 (1995).
28. Mertens, B. M., Overwijk, M. H. F. & Kruit, P. Off-axis holography with a crystal beam splitter. *Ultramicroscopy* **77**, 1–11 (1999).
29. Jönsson, C. Elektroneninterferenzen an mehreren künstlich hergestellten Feinspalten. *Zeitschrift fur Physik* **161**, 454–474 (1961).
30. Gronniger, G. *et al*. Electron diffraction from free-standing, metal-coated transmission gratings. *Applied Physics Letters* **87**, 1–3 (2005).
31. Gronniger, G., Berwick, B. & Batelaan, H. A three-grating electron interferometer. *New Journal of Physics* **8** (2006).
32. Bach, R., Gronniger, G. & Batelaan, H. An electron Talbot-Lau interferometer and magnetic field sensing. *Applied Physics Letters* **103**, 254102 (2013).
33. Missiroli, G. F., Pozzi, G. & Valdre, U. Electron interferometry and interference electron microscopy. *Journal of Physics E: Scientific Instruments* **14**, 649 (1981).
34. Freiberg, A. T. & Sudol, R. J. Propagation Parameters of Gaussian Schell-Model Beams. *Optics Communications* **41**, 383–387 (1982).
35. McMorran, B. & Cronin, A. Gaussian Schell Source as Model for Slit-Collimated Atomic and Molecular Beams. *e-print arXiv:0804.1162v1 (*2008).
36. McMorran, B. & Cronin, A. D. Model for partial coherence and wavefront curvature in grating interferometers. *Physical Review A - Atomic, Molecular, and Optical Physics* **78**, 1–10 (2008).
37. Dronyak, R. *et al*. Electron diffractive imaging of nano-objects using a guided method with a dynamic support. *Applied Physics Letters* **95**, 111908 (2009).
38. Morishita, S., Yamasaki, J. & Tanaka, N. Measurement of spatial coherence of electron beams by using a small selected-area aperture. *Ultramicroscopy* 10–17 (2013).
39. Carter, C. B. & Williams, D. B. (eds.) *Transmission Electron Microscopy - Diffraction, Imaging, and Spectrometry* (Springer).
40. Mertens, B. & Kruit, P. Results of a pilot experiment on direct phase determination of diffracted beams in TEM. In *Electron Microscopy and Analysis Group Conf. EMAG99, Sheffield*, 133–136 (1999).
41. Williams, D. B. & Carter, C. B. *Transmission electron microscopy- A Textbook for Materials Science* (Springer).
42. Simpson, J. A. The theory of the three-cyrstal electron interferometer. *Rev. Sci. Instrum.* **25**, 1105 (1954).
43. McMorran, B. J. & Cronin, A. D. An electron Talbot interferometer. *New Journal of Physics* **11**, 033021 (2009).
44. Cronin, A. D., Schmiedmayer, J. & Pritchard, D. E. Optics and interferometry with atoms and molecules. *Reviews of Modern Physics* **81**, 1051–1129 (2009).
45. Oberthaler, M., Bernet, S., Rasel, E., Schmiedmayer, J. & Zeilinger, A. Inertial sensing with classical atomic beams. *Physical Review A* **54**, 3165–3176 (1996).
46. Elitzur, A. & Vaidman, L. Quantum mechanical interaction-free measurements. *Foundations of Physics* **23**, 987 (1993).
47. Kruit, P. *et al*. Designs for a quantum electron microscope. *Ultramicroscopy* **164**, 31–45 (2016).
48. Kwiat, P., Weinfurter, H., Herzog, T., Zeilinger, A. & Kasevich, M. A. Interaction-Free Measurement. *Physical Review Letters* **74**, 4763–4766 (1995).
49. Wang, J., Pitt, K. & Milgie, M. Multiple interferometer interaction free measurement using polarized light. *Journal of Physics B: Atomic, Molecular and Optical Physics* **49**, 045501 (2016).
50. Tavabi, A. H., Duchamp, M., Grillo, V., Dunin-Borkowski, R. E. & Pozzi, G. New experiments with a double crystal electron interferometer, Forthcoming article. *Eur. Phys. J. Appl. Phys*. (2017).

Acknowledgements

The authors would like to acknowledge helpful discussions and feedback from Pieter Kruit, Mark Kasevich, Peter Hommelhoff, Vitor Manfrinato, Jo Verbeek, Ivan Lobato, and Ricardo Egoavil. The authors would also like to thank Stijn van Den Broeck for FIB fabrication of the two-grating interferometers. Some of the experiments were conducted using microscopy facilities at EMAT, University of Antwerp. This work also made use of the Shared Experimental Facilities supported in part by the MRSEC Program of the National Science Foundation under award number DMR-1419807. This work was supported by the Gordon and Betty Moore Foundation. C.S.K. would like to acknowledge the National Research Foundation of Korea (NRF) grant funded by the Korea government(MEST) (No. 2013R1A6A3A03065200).

Author Contributions

A.A., C.S.K., R.H., and K.K.B. conceived the experiments; A.A. and C.S.K. conducted the experiments. D.V.D. developed the mechanism for electron diffraction from multi-gratings. All authors analyzed the results and reviewed the manuscript.

Additional Information

Supplementary information accompanies this paper at doi:10.1038/s41598-017-01466-0

Competing Interests: The authors declare that they have no competing interests.

Publisher's note: Springer Nature remains neutral with regard to jurisdictional claims in published maps and institutional affiliations.